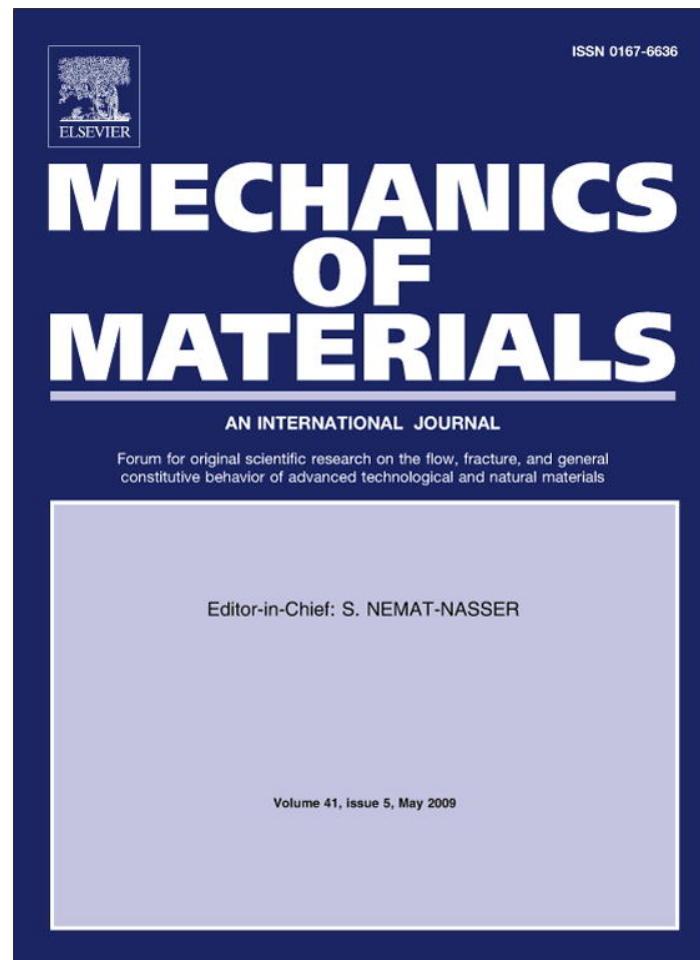


Provided for non-commercial research and education use.
Not for reproduction, distribution or commercial use.



This article appeared in a journal published by Elsevier. The attached copy is furnished to the author for internal non-commercial research and education use, including for instruction at the authors institution and sharing with colleagues.

Other uses, including reproduction and distribution, or selling or licensing copies, or posting to personal, institutional or third party websites are prohibited.

In most cases authors are permitted to post their version of the article (e.g. in Word or Tex form) to their personal website or institutional repository. Authors requiring further information regarding Elsevier's archiving and manuscript policies are encouraged to visit:

<http://www.elsevier.com/copyright>



Contents lists available at ScienceDirect

Mechanics of Materials

journal homepage: www.elsevier.com/locate/mechmat

Multi-scale modeling of heterogeneous adhesives: Effect of particle decohesion

Mohan G. Kulkarni^a, Philippe H. Geubelle^{a,*}, Karel Matouš^{a,b}

^a Department of Aerospace Engineering, 306 Talbot Lab., University of Illinois at Urbana-Champaign, 104 South Wright Street, Urbana, IL 61801, USA

^b Computational Science and Engineering, University of Illinois at Urbana-Champaign, Urbana, IL 61801, USA

ARTICLE INFO

Article history:

Received 17 March 2008

Received in revised form 16 October 2008

ABSTRACT

We examine the microscopic toughening mechanisms and their effect on the macroscopic failure response of heterogeneous adhesives made of stiff particles embedded in a more compliant matrix. The analysis relies on a multi-scale cohesive framework first described in Matouš et al. [Matouš, K., Kulkarni, M., Geubelle, P., 2008. Multiscale cohesive failure modeling of heterogeneous adhesives. *Journal of the Mechanics and Physics of Solids* 56, 1511–1533]. Two microscopic constitutive failure models are incorporated: an isotropic damage model to capture the fracture response of the matrix and a cohesive law to model the inclusion-matrix interfacial debonding. A detailed study of the RVE size is presented followed by a set of examples that illustrate the effect of filler size, volume fraction and particle-matrix interface properties on the macroscopic effective traction-separation law of heterogeneous adhesives.

© 2009 Published by Elsevier Ltd.

1. Introduction

The highly cross-linked and amorphous microstructure of epoxy polymers provides relatively high failure strength and elastic modulus, but makes them inherently brittle and susceptible to fracture. The addition of second-phase micro-heterogeneities such as rubber particles (Pearson and Yee, 1991; Chen and Mai, 1998) and glass beads (Spanoudakis and Young, 1984a; Kitey and Tippur, 2005a) has long been considered to improve fracture properties of thermosetting polymers. A vast body of literature is devoted to the characterization of macroscopic failure properties of epoxy-based particulate composites by studying the micro-toughening mechanisms (Lange, 1970; Johnsen et al., 2007). Of particular relevance to the present work are the articles by Nakamura et al. (1999), Spanoudakis and Young (1984a,b), Kitey and Tippur (2005a,b), Kawaguchi and Pearson (2003a,b) who study the effect of filler size, volume fraction, and particle-matrix

interface adhesion strength on the macroscopic failure properties of stiff particle modified bulk epoxy composites. While some literature exists on the characterization and failure of soft (rubber) particle modified epoxy adhesives (Kinloch, 2003; Pucciariello et al., 1989), the use of stiff particles in epoxy adhesives, which are generally known to have quite different toughening mechanisms than the former, is still relatively uncommon.

The failure of an adhesive can be characterized into two types: *adhesive*, where failure is along the interface between the adhesive and the adherend, and *cohesive*, where failure is contained within the adhesive layer. It has been experimentally recognized that the modification of neat epoxy adhesives by carbon nano-tubes (Hsiao et al., 2003) and rubber particles (Kinloch, 2003) leads to changes in the failure type by introducing several microscopic fracture toughening mechanisms, such as micro-cracking, crack bridging/deflection/pinning and fiber pull-out. In general, heterogeneous adhesives tend to fail in a more cohesive fashion than neat polymer adhesives. From a mechanical design viewpoint, it is important to understand the link between the failure type of an adhesive

* Corresponding author. Tel.: +1 217 244 7648; fax: +1 217 244 0720.
E-mail address: geubelle@uiuc.edu (P.H. Geubelle).

and several design parameters at one's disposal. The study of various failure mechanisms present at the micro-scale and their impact on the macroscopic failure response of the adhesive system is the topic of this paper. In particular, we analyze the effect of particle size, volume fraction, and particle–matrix interface properties on the failure type and effective macroscopic property response of stiff particle reinforced epoxy adhesives using a multi-scale numerical scheme.

At the macro-scale, the cohesive finite element (CFE) method, which collapses the adhesive layer to a surface (in 3D) or a line (in 2D), is a natural choice for numerical analyses of bonded structures. Although attractive for their simplicity, the phenomenological and/or mathematically convenient cohesive laws proposed in the literature do not directly represent the complex failure processes occurring at the micro-level in heterogeneous adhesives. Common examples of such cohesive laws include bi-linear (Geubelle and Baylor, 1998) and exponential (Needleman, 1990b) relations that describe the tractions acting along the crack faces as a function of displacement jump. The extraction of macro-scale cohesive law of heterogeneous adhesives directly from micro-scale simulations is limited due to the complexity of failure processes at that level. A step in that direction was recently achieved by Matouš et al. (2008), who proposed a multi-scale cohesive scheme with an ability to relate the microscopic failure details in heterogeneous layers to the macroscopic traction-separation law. In this paper, we use the multi-scale cohesive approach to analyze the physics of failure processes at micro-scale in heterogeneous layers, with emphasis on the key role played by the particle–matrix interface.

The paper is organized as follows: in Section 2, we summarize the multi-scale cohesive approach. Section 3 describes the constitutive models adopted to simulate the micro-scale failure processes followed, in Section 4, by a brief explanation of the numerical implementation of the scheme. In Section 5, we present a study of the RVE size and a set of illustrative examples.

2. Variational framework for multi-scale scheme

We summarize in this section the multi-scale cohesive model proposed by Matouš et al. (2008) in a variational framework using the formalism of Miehe (2002). Consider $\Omega \subset \mathfrak{R}^3$ to be an open bounded set with a piecewise smooth boundary Γ . Any generic point $\bar{\mathbf{x}}$ is defined by its position vector directed from the origin of \mathfrak{R}^3 . The boundary Γ is assumed to be decomposed into non-intersecting sub-domains Γ_u and Γ_t where displacements and tractions are imposed, respectively. Let the sub-manifold $\Gamma_c \in \mathfrak{R}^2$ with unit normal \mathbf{N} represent a heterogeneous adhesive layer, which divides Ω into two disjoint sets Ω^+ and Ω^- . Let $\Omega^0 = l_c \Gamma_c$ denote the physical volume of the heterogeneous adhesive layer where l_c represents the average thickness of the layer. We assume the adhesive layer repeats itself in the $x_{1,2}$ direction with Θ representing the volume of the periodic heterogeneous unit cell (see Fig. 1).

Let $\mathbf{u}(\mathbf{x})$ represent the displacement field in the heterogeneous microstructure of adhesive layer at a point

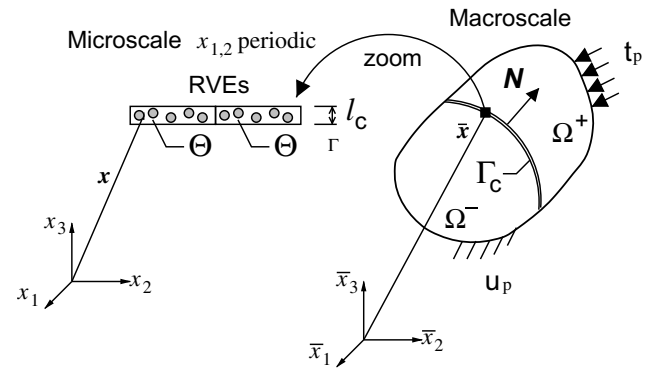


Fig. 1. Multi-scale cohesive approach showing the macro- and micro-scale coupling.

$\mathbf{x} \in \Theta \subset \mathfrak{R}^3$. In what follows, all the quantities with a bar overhead ($\bar{\bullet}$) are defined at the macro-scale, while the perturbation quantities at the micro-scale are denoted with a tilde overhead ($\tilde{\bullet}$). The displacement is assumed to be decomposed into a homogeneous part due to the prescribed macroscopic strain $\bar{\epsilon}$ and a fine-scale fluctuation displacement $\tilde{\mathbf{u}}(\mathbf{x})$ as

$$\mathbf{u}(\mathbf{x}) = \bar{\epsilon}\mathbf{x} + \tilde{\mathbf{u}}(\mathbf{x}). \quad (1)$$

The microscopic strain field is then given by the symmetric part of the gradient of displacement field as

$$\epsilon(\mathbf{x}) = \nabla^s \mathbf{u}(\mathbf{x}) = \bar{\epsilon} + \tilde{\epsilon}(\mathbf{x}), \quad (2)$$

which constitutes an additive decomposition into a homogeneous macroscopic part $\bar{\epsilon}$ and a fluctuation part $\tilde{\epsilon} = \nabla^s \tilde{\mathbf{u}}(\mathbf{x})$. The macroscopic strain is assumed to be governed by surface data of the microscopic displacement field (Hill, 1972) as

$$\bar{\epsilon} = \frac{1}{|\Theta|} \int_{\partial\Theta} (\mathbf{u} \otimes \mathbf{n})^s dA, \quad (3)$$

where \mathbf{n} represents the normal to the boundary of micro-structure, the symbol \otimes denotes vector dyadic product and the operator $(\bullet)^s$ yields the symmetric part of a second-order tensor. Condition (3) places the following restriction on the fluctuation field $\tilde{\mathbf{u}}$ in decomposition (1):

$$\frac{1}{|\Theta|} \int_{\partial\Theta} [\tilde{\mathbf{u}} \otimes \mathbf{n}] dA = 0. \quad (4)$$

Let Ψ denote the stress potential at the micro-scale that relates the stress to the strain in the adhesive layer $\sigma = \partial_\epsilon \Psi(\epsilon, \mathbf{x})$. To bridge the macro- and micro-scales, we introduce the minimization relation given by modified Hill's lemma (see Matouš et al., 2008 for details)

$$\inf_{\bar{\epsilon}} \bar{\Psi}(\bar{\epsilon}) = \inf_{\bar{\epsilon}} \inf_{\tilde{\mathbf{u}}} \frac{l_c}{|\Theta|} \int_{\Theta} \Psi(\bar{\epsilon} + \nabla^s \tilde{\mathbf{u}}) d\Theta, \quad (5)$$

where $\bar{\Psi}$ is the macro-traction potential that by recourse to the Coleman and Noll's method (Lubliner, 1972, 1973) yields the cohesive law describing the failure of the adhesive layer at the macro-scale, i.e., $\bar{\mathbf{t}} = \frac{\partial \bar{\Psi}}{\partial \bar{\mathbf{u}}}$. $\bar{\mathbf{u}}$ denotes the macroscopic displacement and the symbol $[\bullet] = (\bullet^+ - \bullet^-)$ represents the jump operator. Constraint (4) can be satisfied

fied for the following two classes of local boundary conditions:

$$(i) \quad \tilde{\mathbf{u}}(\mathbf{x}) = \mathbf{0} \quad \text{on } \partial\Theta \quad \text{and} \quad (ii) \quad \tilde{\mathbf{u}}^+(\mathbf{x}) = \tilde{\mathbf{u}}^-(\mathbf{x}) \quad \text{on } \partial\Theta. \quad (6)$$

Together with (1), the first condition leads to linear displacements on the boundary of the microstructure, while the second condition implies periodicity of the microstructure. For the thin adhesive layer, we satisfy condition (4) using a combination of the two purely kinematic conditions (6)

$$\tilde{\mathbf{u}} \in \mathcal{V} := \left\{ \tilde{\mathbf{u}} | \tilde{\mathbf{u}} \in H^1(\Theta), \tilde{\mathbf{u}} - x_{1,2} \text{ periodic}, \tilde{\mathbf{u}}|_{\Gamma_c^\pm} = \mathbf{0} \right\}, \quad (7)$$

where $H^1(\Theta) = \{ \tilde{\mathbf{u}} | \tilde{\mathbf{u}} \in L_2; \tilde{\mathbf{u}}_i \in L_2 \}$ with L_2 being the space of square-integrable functions over Θ . To satisfy the minimization problem (5), we require that the variations with respect to the strain $\delta\bar{\epsilon}$ and virtual fluctuation field $\delta\tilde{\mathbf{u}}$ vanish independently so that

$$\bar{\mathbf{t}} \cdot [\delta\tilde{\mathbf{u}}] = \frac{l_c}{|\Theta|} \int_{\Theta} \boldsymbol{\sigma} d\Theta : \delta\bar{\epsilon} \quad \text{at the macro-scale}, \quad (8)$$

$$\frac{1}{|\Theta|} \int_{\Theta} \nabla \delta\tilde{\mathbf{u}} : \boldsymbol{\sigma} d\Theta = 0 \quad \text{at the micro-scale}. \quad (9)$$

Exploiting the arbitrariness of the macroscopic strain field, we let $\delta\bar{\epsilon} = \frac{1}{l_c} (\mathbf{N} \otimes \delta[\tilde{\mathbf{u}}])^s$, which, along with (8) and arbitrariness of $[\delta\tilde{\mathbf{u}}]$, leads to the macroscopic cohesive traction vector

$$\bar{\mathbf{t}} = \frac{1}{|\Theta|} \int_{\Theta} \boldsymbol{\sigma} d\Theta \cdot \mathbf{N}. \quad (10)$$

Eq. (9) is the weak form of the momentum balance at the micro-scale, which can be solved along with the local boundary conditions (7). Further, the macroscopic strain field in the heterogeneous adhesive layer is approximated in terms of the macroscopic displacement jump vector $[\tilde{\mathbf{u}}]$ as

$$\bar{\epsilon} := \frac{1}{l_c} (\mathbf{N} \otimes [\tilde{\mathbf{u}}])^s. \quad (11)$$

Without loss of generality, we can consider the adhesive layer to be in the $x_3 = 0$ plane, for which (11) reduces to

$$\bar{\epsilon} = \frac{1}{l_c} \begin{bmatrix} 0 & 0 & \frac{1}{2} [\tilde{u}_1] \\ 0 & 0 & \frac{1}{2} [\tilde{u}_2] \\ \frac{1}{2} [\tilde{u}_1] & \frac{1}{2} [\tilde{u}_2] & [\tilde{u}_3] \end{bmatrix}. \quad (12)$$

3. Constitutive response

We now describe the constitutive models adopted in this work (i) to model the behavior of the constituents of the heterogeneous adhesive, and (ii) to capture the inclusion-matrix interface debonding.

3.1. Irreversible damage model

The damage model employs irreversible thermodynamics and the internal state variables theory (Simo and Ju,

1987a). To introduce damage, let us consider the free energy potential given by

$$\Phi(\epsilon, \omega) = (1 - \omega)\Phi_0(\epsilon), \quad (13)$$

with

$$\Phi_0(\epsilon) = \frac{1}{2} \epsilon : \mathbf{L}(\mathbf{x}) : \epsilon, \quad (14)$$

where $\Phi_0(\epsilon)$ represents the total potential energy function of an undamaged (virgin) material, ω denotes the isotropic damage parameter and $\mathbf{L}(\mathbf{x})$ is the elastic stiffness of microconstituents.

The onset of damage is defined based on the concept of damage surface. The state of damage in the material is governed by

$$g(Y, \chi^t) = G(Y) - \chi^t \leq 0, \quad \mathbf{t} \in \mathbb{R}^+, \quad (15)$$

where Y is the thermodynamic force or damage energy release rate, while χ^t denotes the softening parameter (internal state variable) usually set as $\chi^t = 0$. The function $G(Y)$ that characterizes the damage process in the material can possess various mathematical forms and we adopt hereafter a three-parameter Weibull distribution that reads

$$G(Y) = 1 - \exp \left[- \left(\frac{Y - Y_{in}}{p_1 Y_{in}} \right)^{p_2} \right], \quad (16)$$

where Y_{in} denotes the initial threshold (energy barrier), and p_1 and p_2 are non-dimensional scale and shape parameters, respectively.

The damage process is derived in terms of the following irreversible, dissipative evolution equations

$$\dot{\omega} = \dot{\kappa} \frac{\partial g}{\partial Y} = \dot{\kappa} H, \quad H = \frac{\partial G(Y)}{\partial Y}, \quad (17)$$

where $\dot{\kappa}$ is the damage consistency parameter, which defines damage loading/unloading according to the Kuhn-Tucker complementarity conditions:

$$\dot{\kappa} \geq 0, \quad g(Y, \chi^t) \leq 0, \quad \dot{\kappa} g(Y, \chi^t) \equiv 0. \quad (18)$$

In addition, we define $\dot{\chi}^t = \dot{\kappa} H$ and the parameter $\dot{\kappa}$ is determined from the consistency condition $\dot{g} = 0$, from which follows

$$\dot{\kappa} = -\dot{Y} \quad \text{and} \quad \dot{Y} = - \frac{\boldsymbol{\sigma}}{(1 - \omega)} : \dot{\epsilon}. \quad (19)$$

The internal state variable evolves in a monotonically increasing fashion and we assume unloading towards the origin. It should be noted that the damage model leads to loss of strong material ellipticity and the associated numerical computations tend to exhibit mesh bias. To address this issue, we adopt the viscous regularization approach proposed by Simo and Ju (1987b). The evolution equations for $\dot{\omega}$ and $\dot{\chi}^t$ that govern the visco-damage behavior are obtained by replacing the damage consistency parameter $\dot{\kappa}$ as

$$\dot{\omega} = \dot{\kappa} H \rightarrow \dot{\omega} = \mu g \quad \text{and} \quad \dot{\chi}^t = \dot{\kappa} H \rightarrow \dot{\chi}^t = g, \quad (20)$$

where μ denotes the damage viscosity coefficient. As μ tends to zero, one recovers the instantaneous elastic behavior, while for μ approaching infinity, the rate-independent response is obtained.

3.2. Irreversible cohesive law

As indicated in Section 1, a key objective of this paper is to study the effect of the properties of inclusion-matrix interface on the type of failure taking place in the adhesive layer and on the resulting macroscopic traction-separation law. To model the failure of the inclusion-matrix interface, we could adopt a cohesive failure law that could itself be a result of another continuum or atomistic multi-scale analysis. In this work, however, we opt for the rate-independent exponential cohesive failure law proposed by Ortiz and Pandolfi (1999). Only the essential details of the model are summarized below.

Denoting by ψ the cohesive free energy density per unit area, we write the cohesive traction vector \mathbf{t}_0 as

$$\mathbf{t}_0 = \frac{\partial \psi}{\partial \boldsymbol{\delta}}, \quad \mathbf{t}_0 = \frac{\hat{\mathbf{t}}}{\hat{\delta}} \mathbf{t}, \quad \mathbf{t} = [\beta^2 \boldsymbol{\delta} + (1 - \beta^2)(\boldsymbol{\delta} \cdot \mathbf{N}_c)\mathbf{N}_c], \quad (21)$$

where $\boldsymbol{\delta} = \tilde{\mathbf{u}}^+ - \tilde{\mathbf{u}}^-$ denotes the displacement jump vector, $\beta \in [0; 1]$ is the mode mixity factor, and \mathbf{N}_c represents the unit normal to the particle-matrix cohesive surface. The effective displacement jump $\hat{\delta}$ is defined as

$$\hat{\delta} = \sqrt{\beta^2 \hat{\delta}_s^2 + \hat{\delta}_n^2}, \quad (22)$$

where $\hat{\delta}_s$ and $\hat{\delta}_n$ denote the sliding and normal displacement jumps, respectively, and are given by

$$\hat{\delta}_s = |\boldsymbol{\delta}_s|, \quad \boldsymbol{\delta}_s = (\mathbf{1} - \mathbf{N}_c \otimes \mathbf{N}_c)\boldsymbol{\delta}, \quad \hat{\delta}_n = \boldsymbol{\delta} \cdot \mathbf{N}_c. \quad (23)$$

In this work, we adopt the simple and computationally convenient exponential cohesive law (Fig. 2) described by

$$\psi = e\hat{\sigma}_c\hat{\delta}_c \left[1 - \left(1 + \frac{\hat{\delta}}{\hat{\delta}_c} \right) \exp\left(\frac{-\hat{\delta}}{\hat{\delta}_c}\right) \right], \quad (24)$$

$$\hat{\mathbf{t}} = \frac{\partial \psi}{\partial \hat{\boldsymbol{\delta}}} = e\hat{\sigma}_c \frac{\hat{\boldsymbol{\delta}}}{\hat{\delta}_c} \exp\left(\frac{-\hat{\delta}}{\hat{\delta}_c}\right), \quad (25)$$

where $e = \exp(1)$, $\hat{\sigma}_c$ denotes the maximum effective cohesive traction and $\hat{\delta}_c$ is the critical effective opening displacement jump beyond which the interface experiences damage. The cohesive fracture energy per unit area, i.e., the area under the traction-separation law \hat{G}_c described by (25), is given by

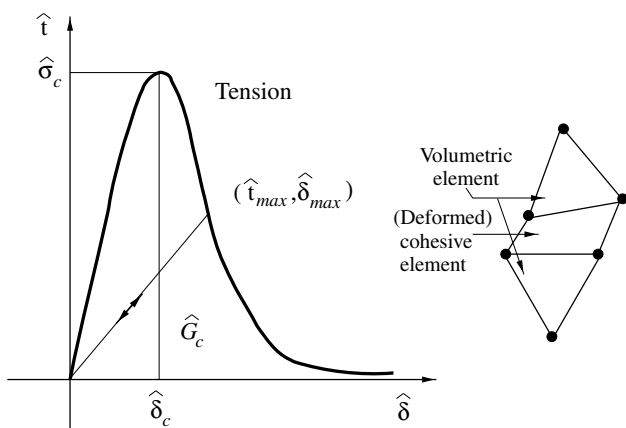


Fig. 2. Schematic of microscopic cohesive element and irreversible cohesive law.

$$\hat{G}_c = \int_0^\infty \hat{t} d\hat{\delta} = e\hat{\sigma}_c\hat{\delta}_c, \quad (26)$$

which relates the material parameters \hat{G}_c , $\hat{\sigma}_c$ and $\hat{\delta}_c$.

The failure processes occurring within the heterogeneous materials are quite complex and involve loading, unloading and contact along the particle-matrix interfaces. This necessitates accurate tracking of the history of failure of cohesive interfaces. The loading/unloading of the internal state variable, $\hat{\delta}_{max}$, is assumed to be similar to the formulation presented in Ortiz and Pandolfi (1999) and is given by

$$\hat{\delta}_{max} = \hat{\delta} \quad \text{if } \hat{\delta} = \hat{\delta}_{max} \quad \text{and} \quad \hat{\delta} \geq 0, \\ = 0 \quad \text{otherwise.} \quad (27)$$

As shown in Fig. 2, the unloading is assumed to be directed towards the origin:

$$\hat{t} = \frac{\hat{t}_{max}}{\hat{\delta}_{max}} \hat{\delta} \quad \text{if } \hat{\delta} < \hat{\delta}_{max}. \quad (28)$$

Upon closure, however, noticing that friction and contact are external to the cohesive law, we separate the normal and shear responses. The shear response under normal closure is assumed to be the same as in opening, while we adopt the following form of the normal traction in order to enforce the contact constraint on the cohesive surfaces:

$$\hat{t}_n = e\hat{\sigma}_c \exp\left(\frac{-\hat{\delta}_{max}}{\hat{\delta}_c}\right) \frac{1}{\alpha} \sinh\left(\frac{\alpha\hat{\delta}_n}{\hat{\delta}_c}\right) \quad \forall \hat{\delta}_n < 0, \quad (29)$$

where α is a dimensionless parameter that controls the growth of compressive normal traction \hat{t}_n ($\alpha = 50$ for the examples considered in this paper). Relation (29) is chosen to be continuously differentiable at origin in the $\hat{t}_n - \hat{\delta}_n$ space even after partial failure of the interface, i.e.,

$$\left[\frac{\partial \hat{t}_n}{\partial \hat{\delta}_n} \right]_{\hat{\delta}_n=0^-} = \left[\frac{\partial \hat{t}_n}{\partial \hat{\delta}_n} \right]_{\hat{\delta}_n=0^+}. \quad (30)$$

4. Numerical implementation

In this paper, we use the finite element method to solve the micro-scale equilibrium (9) subject to purely kinematic boundary conditions (6) and an imposed macroscopic displacement jump $[\tilde{\mathbf{u}}]$ to obtain the macroscopic tractions (10). To solve the micro-scale equilibrium problem, we decompose the micro-scale domain Θ into open, non-overlapping subdomains, denoted by Θ^e , $e = 1, 2, \dots, n_{ele}$. The weak form of the equilibrium on the micro-scale (9) can be discretized to obtain the non-linear finite element form as

$$\mathfrak{R}(\tilde{\mathbf{U}}) \equiv \frac{1}{|\Theta^e|} \sum_{e=1}^{n_{ele}} \left\{ \underbrace{\int_{\Theta^e} [\mathbf{B}]^T \{\boldsymbol{\sigma}\} d\Theta^e}_{\text{volumetric contribution}} + \underbrace{\int_{\Gamma_{coh}^e} [\mathbf{P}]^T \mathbf{t}_0 d\Gamma^e}_{\text{interfacial contribution}} \right\} = \mathbf{0}, \quad (31)$$

where $[\mathbf{B}]$ represents the standard finite element strain-displacement matrix, while Γ_{coh}^e denotes the inclusion-matrix cohesive interface. The $[\mathbf{P}]$ matrix in the interfacial

contribution involves standard one-dimensional shape functions. The symbol \mathbb{A} in (31) denotes the finite element assembly operator, and we adopt Voigt notation to represent the symmetric stress tensor at the micro-scale as $\{\sigma\} = (1 - \omega)[\mathbf{L}]\{\bar{\epsilon} + \tilde{\epsilon}\}$. The term involving the macroscopic strain $\bar{\epsilon}$ acts as the external force at the micro-scale, while the internal force consists of the fluctuating strain $\tilde{\epsilon}$ and the interfacial contribution. The micro-scale set of non-linear equations (31) are solved for the micro-scale degree-of-freedom vector, $\tilde{\mathbf{U}}$, using Newton–Raphson iterative solution procedure. The consistent tangent is implemented in the numerical framework, which ensures the optimal quadratic rate of convergence. The numerical integration of the rate form of damage constitutive equations is carried out using the backward Euler scheme (Matouš et al., 2008).

The high initial stiffness of the cohesive elements, coupled with loss of matrix integrity due to damage evolution, poses convergence difficulties for the numerical solution. Several loading/unloading events occurring due to the damage localization in matrix, particle debonding and contact along the particle–matrix interface further exacerbate the convergence issues. We have adopted an adaptive time-stepping procedure that allows us to vary the loading step size without losing accuracy. The procedure is based on the value of maximum increment in the damage parameter ($\Delta\omega$) or cohesive internal variable ($\Delta\delta_{max}$) at any integration point (see Matouš et al., 2008 for more details). In addition, as discussed in Section 3.2, the normal and shear response for the particle–matrix interface behavior are separated upon closure. We also impose constraint (30) to enforce the continuity of derivatives at the origin in $\hat{t}_n - \hat{\delta}_n$ space.

5. Results and discussion

Although the formulation presented in the previous sections is 3D, all the examples discussed hereafter are solved in a 2D plane strain setting. The macroscopic loading rate is kept constant for all loading cases (mode I or mixed mode) such that $\dot{\bar{\epsilon}}_{33} = 0.1 \text{ s}^{-1}$, $\dot{\bar{\epsilon}}_{23} = 0.1 \text{ s}^{-1}$ and $[\bar{u}_2]/[\bar{u}_3] = 1.0$ for mixed loading. The material properties chosen for the examples are listed in Table 1. The damage evolution of a simulated brittle epoxy matrix is captured using the isotropic damage model described in Section 3.1. The damage viscosity entering (20) is chosen as $\mu = 19.0 \text{ s}^{-1}$ in the remainder of the manuscript. This value is chosen to eliminate the mesh bias of the finite element solution, while providing a brittle behavior for the epoxy matrix for the specified macroscopic strain rate. The inclusions are assumed to have a linear elastic response and are 10 times stiffer than the matrix. This essentially simulates the response of stiff particles in a compliant-brittle matrix.

Table 1
Material properties for stiff particle/soft matrix example.

	E (GPa)	ν	Y_m (N/mm ²)	p_1	p_2	μ (1/s)
Matrix	2.4	0.34	0.32	2.5	8.0	19.0
Inclusion	24.0	0.34	–	–	–	–

The interface properties ($\hat{\sigma}_c = 50 \text{ MPa}$, $\hat{\delta}_c = 0.0026 \text{ mm}$, $\beta = 0.8$) are chosen in such a way that the interface failure strength $\hat{\sigma}_c$ is lower than the maximum matrix strength and complete interface failure occurs within the applied range of loading. In all the examples presented hereafter, it is made sure that the finite element solution is spatially and temporally converged. In the remainder of this section, we first present the study of RVE size and later focus our attention on analyzing the effect of particle size, volume fraction, and inclusion–matrix interface properties on the microscopic failure details and macroscopic traction-separation law of heterogeneous adhesives.

5.1. RVE size

To be representative, the RVE should be large enough to contain sufficient information about the microstructural geometry and failure events, but small enough so that the argument of scale separation is applicable and computational analysis is feasible. The question of existence and size of RVE is relatively unanswered for brittle materials with strong softening (Gitman et al., 2007). In order to investigate the size of RVE, we consider eight different values of RVE width w ranging from 150 to 4000 μm , while maintaining the RVE height ($l_c = 300 \mu\text{m}$), particle size ($\phi = 80 \mu\text{m}$), and volume fraction ($V_f = 22.34\%$) constant. The choice RVE height is motivated by practical size of adhesive films. The values of ϕ and V_f correspond to the reference problem analyzed in this study. The statistical effect of particle distribution is taken into account by considering 10 randomly oriented microstructural realizations for each RVE width. The macroscopic traction-separation curves for a few representative cases (3 of 8) under mixed-mode loading are shown in Fig. 3. Here, we highlight the fact that it usually suffices to perform the representativeness study under mixed-mode loading, when the effective properties are more sensitive to the effect of semi-periodic boundary conditions than under the mode I loading. However, legitimate conclusions about the RVE size can be obtained only

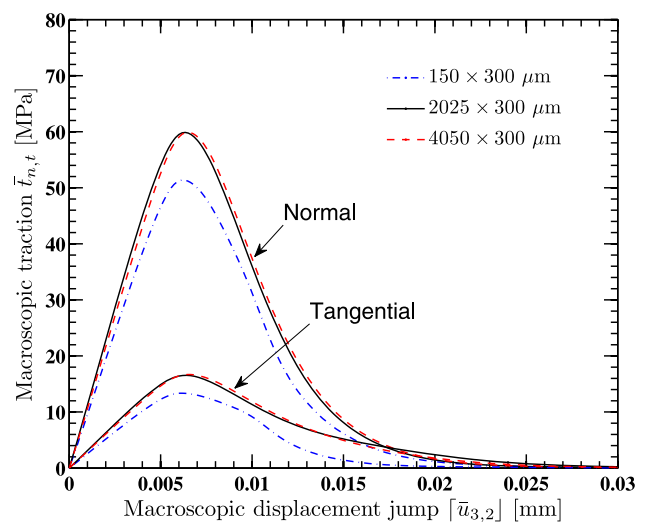


Fig. 3. Effect of RVE size on the macroscopic traction-separation curve under mixed-mode loading.

by computing the bounds. The macroscopic curves correspond to the mean of the 10 different particle realizations. For $w \geq 2000 \mu\text{m}$, the macroscopic curves are indistinguishable under mixed-mode loading. The effect of RVE width on the macroscopic mode I adhesive fracture toughness \bar{G}_{Ic} and failure strength $\bar{\sigma}_{max}$ is depicted in Fig. 4(a) and (b), respectively. The curves correspond to the mean, while the size of the error bars is given by standard deviation of the 10 random realizations. The fracture toughness is computed by evaluating the area under macroscopic traction-separation curve as

$$\bar{G}_{I/IIc} = \int_0^{[\bar{u}]_f} \bar{t}_{n,t}([\bar{\mathbf{u}}]) d[\bar{u}_{3,2}], \quad (32)$$

where $\bar{G}_{I/IIc}$ denotes the mode I or mode II fracture toughness and $[\bar{u}]_f$ is the displacement jump associated with the complete failure of the adhesive layer. The peak stress in macroscopic traction-separation curve is designated as failure strength. As shown in Fig. 4(a) and (b), the mean values of \bar{G}_{Ic} and $\bar{\sigma}_{max}$ become insensitive to the RVE width for $w \geq 500 \mu\text{m}$, with the error bars becoming small for

$w \geq 3000 \mu\text{m}$. In the remainder of the examples presented in this paper, we choose a conservative value of $w = 3000 \mu\text{m}$, so as to have a sufficiently large domain to analyze the micro-scale failure details, although a width of about $1000 \mu\text{m}$ would be most likely sufficient to obtain the effective macroscopic properties.

To conclude this section on the RVE size study, let us emphasize that a more rigorous analysis of RVE size that takes into account a wide range of volume fractions, particle size and elastic property mismatch would be necessary in order to determine the representative dimensions applicable for a general class of brittle materials that exhibit softening.

5.2. Effect of particle size

Five representative cells having equal volume fraction ($V_f = 22.34\%$) and containing 10, 15, 21, 40, and 103 particles of diameter $\phi = 160.0, 130.7, 110.4, 80.0,$ and $50.0 \mu\text{m}$, respectively, are chosen to study the effect of the particle size on the failure of the adhesive system. The effect of particle size on the macroscopic constitutive

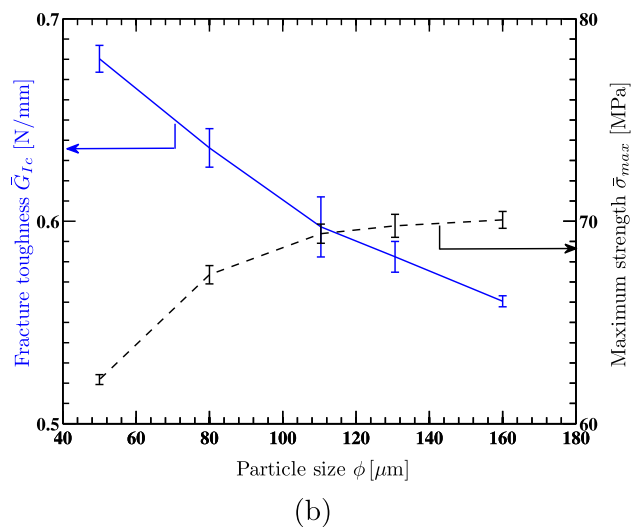
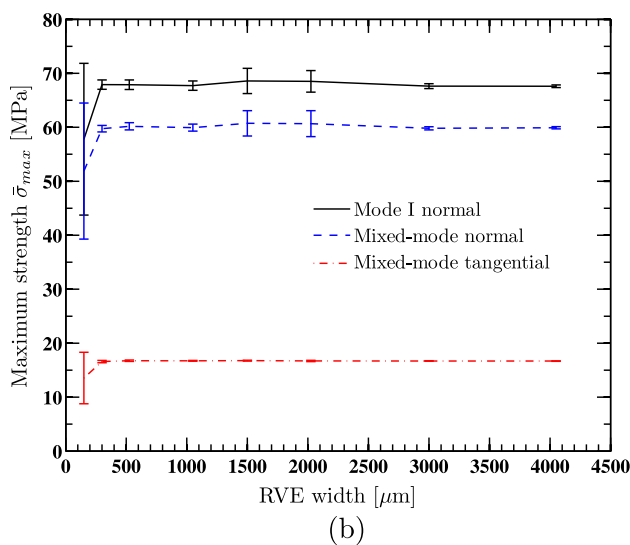
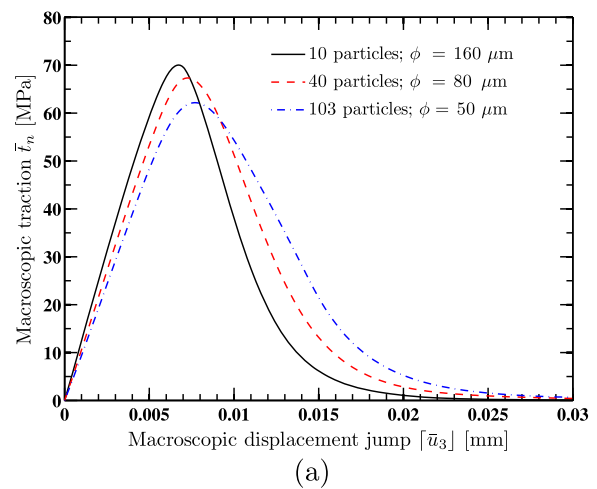
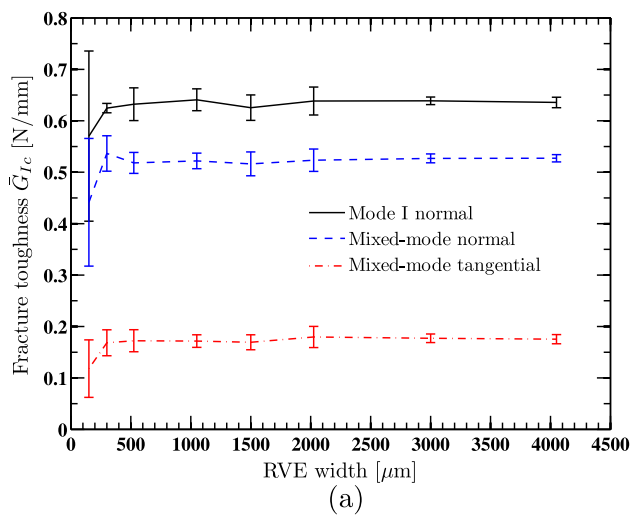


Fig. 4. Effect of RVE size on mode I and mixed-mode fracture toughness (a) and failure strength (b).

Fig. 5. Effect of particle size on macroscopic traction-separation curve (a) and macro-scale fracture toughness and failure strength (b) under mode I loading.

law is presented in Fig. 5(a). Since the number of cohesive surfaces across the particle–matrix interface increases with increase in the number of particles, the slope of the macroscopic traction-separation curve in the initial linear regime decreases. This is due to the intrinsic nature of the adopted cohesive law, i.e., the cohesive surfaces contribute to the apparent stiffness of the heterogeneous adhesive. The failure process gets delayed with decrease in particle size leading to a shift of the softening (downward) part of the macroscopic cohesive curve to higher displacement jump values. As before, the macroscopic failure properties, namely, the mode I fracture toughness \bar{G}_{Ic} and failure strength $\bar{\sigma}_{max}$ can be extracted from the traction-separation law (Fig. 5(b)). The error bars represent the standard deviation computed for five random particle realizations. Increasing the particle size results in a higher failure strength. The prolonged failure for smaller particle sizes, on the other hand, results in an exactly opposite trend for the fracture toughness, in general agreement with the experimental observations reported by Spanoudakis and Young (1984a) for lower volume fractions. The effect of particle size on macroscopic properties is more pronounced for smaller particles than for larger ones.

The damage pattern at complete failure for three cases are shown in Fig. 6(a)–(c). We observe that some of micro-cracks that initiate at the particle–matrix interface are arrested, while others coalesce together to form a dominant macrocrack leading to complete failure of the heterogeneous layer. The dominant macrocrack is formed by the

combination of matrix failure and particle–matrix interface debonding. Similar fracture surfaces consisting of matrix microcracking and particle–matrix debonding has been reported in Kawaguchi and Pearson (2003b) for glass-filled epoxy. Overall, the crack propagation direction is perpendicular to the macroscopic loading. The damage zone in the matrix is about 6–8 elements thick. The large damage zones observed in Fig. 6 are an effect of strain concentration in the damaged elements on the deformed mesh. Fig. 6(b) also shows a more detailed view of damage in the vicinity of two debonded particles. The amount and location of debonding is associated not only with the macroscopic loading direction (right zoomed view) but also with the interaction with neighboring particles (left zoomed view). Furthermore, we notice that, with decrease in the particle size, the damage pattern is more distributed, which explains the associated increase in the fracture toughness.

Fig. 6(d) shows the damage pattern for the 40-particles case with perfect particle–matrix interface. The material properties for the matrix and inclusions are exactly the same as before (Table 1), but no cohesive elements are introduced along the particle–matrix interfaces. By contrasting Fig. 6(b) and (d), we see that the failure is completely cohesive in the former case, while it is adhesive–cohesive in the latter. In the present study, where no particular model is introduced to capture the behavior at the interface between adhesive and adherends, adhesive failure refers to damage inside the matrix in the vicinity of adherend, while cohesive failure alludes to fracture well inside the heterogeneous layer. Restricting the failure to cohesive type could be of particular importance in designing adhesives that are usually considered as a weak link in the bonded structure and are susceptible to interfacial or adhesive failure. Thus, controlling the particle–matrix interface properties may play an important role in deciding the failure type of an adhesive.

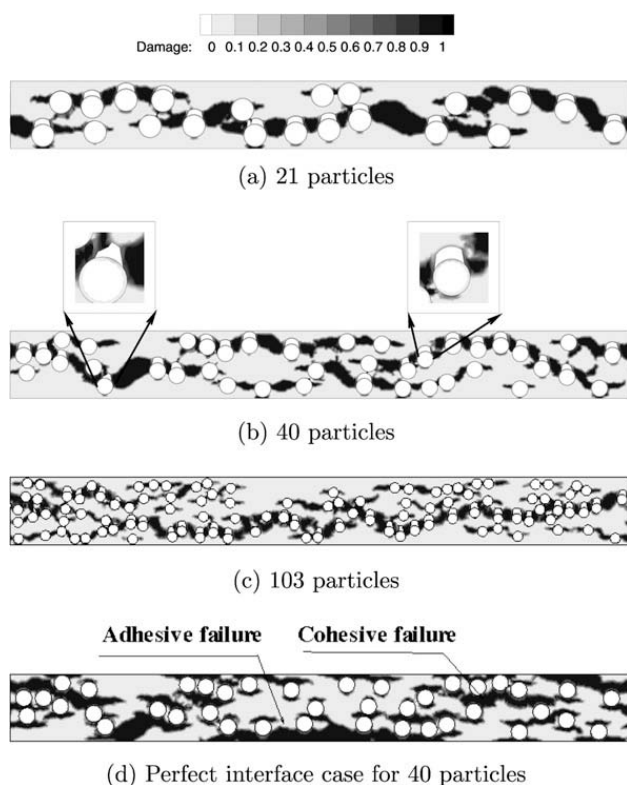


Fig. 6. Effect of particle size on micro-scale damage pattern under mode I loading. The contours correspond to values of the damage parameter ω introduced in (13). The results are displayed on the deformed mesh.

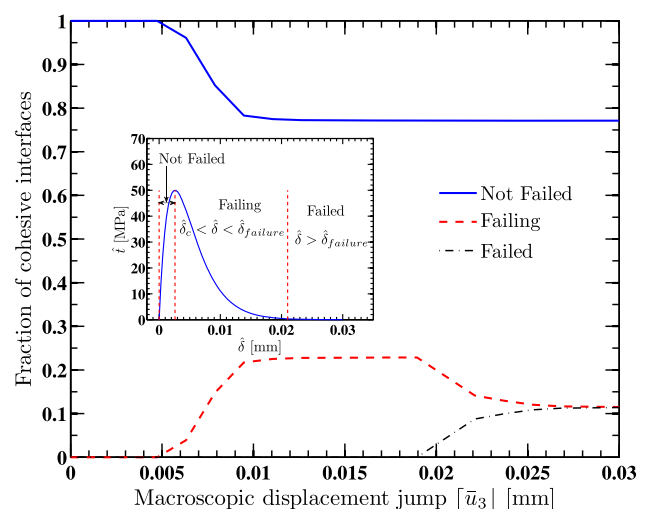


Fig. 7. Fraction of cohesive interfaces not failed, failing, and failed as a function of loading history for 40-particles case under mode I loading. The inset of the figure shows the characterization of a cohesive interface into different categories based on the value of the particle–matrix displacement jump δ .

To gain some insight on the evolution and extent of the particle–matrix interfacial debonding, we focus in Fig. 7 on the failure status of cohesive interfaces as a function of loading history for the 40-particles case under mode I loading. For a macroscopic loading $[\bar{u}_3] > 0.005$ mm, about 25% of the cohesive interfaces start to fail leading to a substantial change in the shape of the macroscopic cohesive law (Fig. 5(a)). Only after sufficient opening is achieved, the fraction of fully failed interfaces becomes non-zero and is accompanied by a reduction in the number of failing interfaces. It is a mere coincidence that the fraction of failing and failed cohesive interfaces asymptote at the same level. It should also be noted that the sum of fractions of cohesive interfaces at any instant of loading is unity.

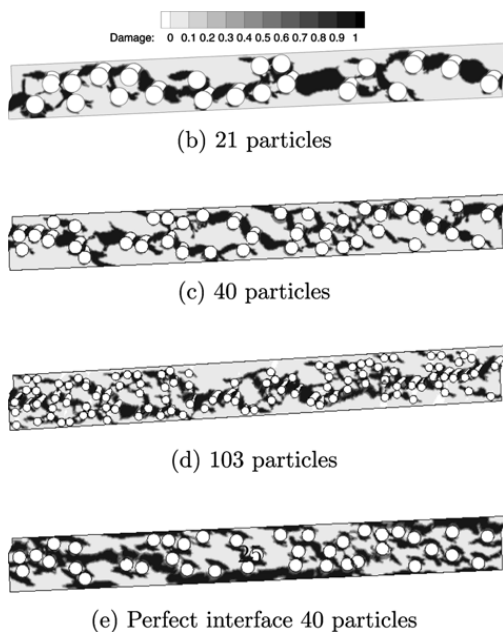
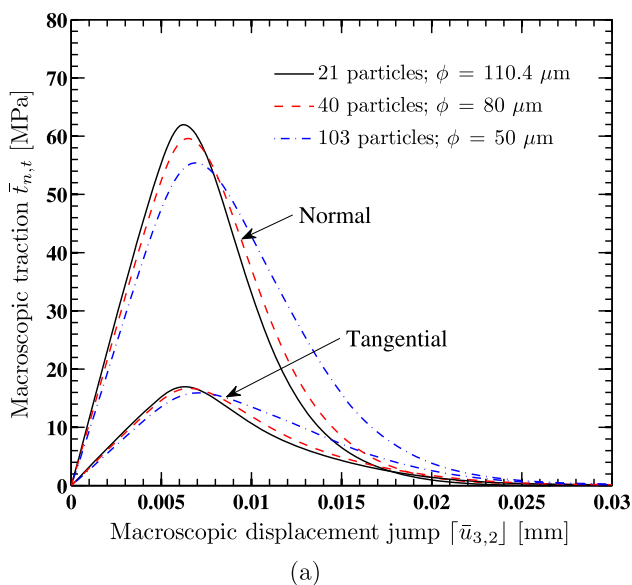


Fig. 8. Effect of particle size on macroscopic traction–separation curve (a) and damage pattern (b)–(e) under mixed-mode loading.

The effect of the particle size on the macroscopic effective properties under mixed-mode loading is illustrated in Fig. 8(a), while the corresponding damage patterns at failure are shown in Fig. 8(b)–(d). As expected, the maximum normal macroscopic tractions are lower than under mode I loading (Fig. 5(a)) due to the coupling between the normal and shear modes. A clear size effect is observed indicating increased fracture toughness with decrease in particle diameter. The damage patterns are much more distributed compared to the mode I loading and the semi-periodicity of the heterogeneous layer is evident under mixed-mode loading. For the 21-particles case (Fig. 8(b)), only one dominant macro-crack is observed, while for the 103-particles case (Fig. 8(d)) several microcracks normal to direction of loading result in a complete failure. The particle debonding is also observed to be normal to the loading direction. Again, as in the mode I case, the failure is completely cohesive or contained within the layer. The damage pattern for the 40-particles perfect interface case under mixed-mode loading, shown in Fig. 8(e), indicates an adhesive–cohesive failure, as opposed to the cohesive failure for the weak interface (Fig. 8(c)).

5.3. Effect of distribution in particle size

As opposed to Section 5.2, where the inclusion diameter within each realization is assumed to be constant, we consider in this section a Gaussian distribution of particle sizes. The mean particle diameter is assumed to be $80 \mu\text{m}$ with the standard deviation (σ) ranging from 0.2 to $15 \mu\text{m}$. The heterogeneity volume fraction (22.34%) and the number of particles (40) are maintained constant. The effect of particle size distribution on the macroscopic cohesive law and damage pattern at failure is depicted in Fig. 9. Although the particle distribution does not show an appreciable effect on the macroscopic cohesive law (Fig. 9(a)), differences can be observed in the microscopic failure pattern (Fig. 9(b)–(d)): the micro-cracks tend to coalesce so as to bridge the bigger size particles, which debond sooner than smaller ones (Nicholson, 1979; Gent, 1980). The macroscopic fracture toughness is, however, hardly affected by the distribution in particle size since the energy dissipated in damaging the matrix is the major factor contributing to fracture toughness as opposed to the change in cohesive failure energy introduced by practical distribution in particle size. The adhesive failure strength, which is dictated by formation of a macro-crack in the matrix, is also independent of the spread in particle size.

5.4. Effect of volume fraction

The effect of volume fraction V_f on the failure characteristics of heterogeneous adhesives is examined using nine different volume fractions ranging from 2.79% to 30.15%, while maintaining the particle diameter constant ($\phi = 80 \mu\text{m}$). The statistical nature of particle distribution is taken into account by considering five random particle realizations for each volume fraction. The effect of volume fraction on the effective traction–separation law of the layer is depicted in Fig. 10(a), which shows the mean of

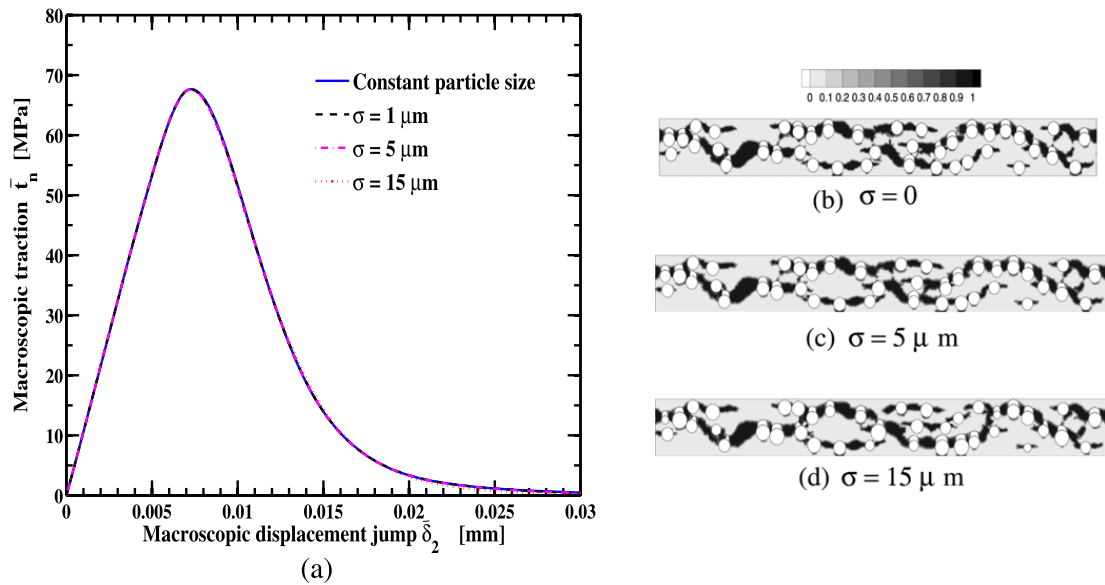


Fig. 9. Effect of variation of particle size on macroscopic traction-separation (a) and on the damage pattern (b)–(d) law under mode I loading.

the five random realizations for four values of V_f . Although the particles are stiffer than the matrix, an increase in the particle volume fraction results in a slight reduction of the slope of the initial linear regime and lower failure strength due to the increased number of weak particle–matrix interfaces. The softening regime of the macroscopic cohesive law is characterized by failure of particle–matrix interfaces and the failure is prolonged with increase in the number of particles.

The macroscopic failure strength $\bar{\sigma}_{max}$ and fracture toughness \bar{G}_{Ic} of the adhesive extracted from the macroscopic traction-separation laws are shown in Fig. 10(b). The error bars are again calculated as standard deviation about mean of five random particle realizations. As pointed out before, the failure strength decreases with increase in particle volume fraction. On the other hand, the fracture toughness increases with higher volume fraction. This can be attributed to the more distributed nature of damage and increasingly higher amount of energy spent in the debonding of particle–matrix interface.

5.5. Effect of micro-scale particle–matrix interface parameters

We now study the effect of the two physical parameters of the cohesive law employed to model the particle–matrix interface failure (Section 3.2), namely, the critical strength $\hat{\sigma}_c$ and fracture toughness \bar{G}_c . The study is performed on five randomly chosen particle realizations consisting of 40 particles of 80 μm diameter constituting a volume fraction of 22.34% under mode I loading. The effect of variation of $\hat{\sigma}_c$, the particle–matrix interface strength, on the macroscopic properties, while maintaining the interface toughness, \bar{G}_c , constant, is presented in Fig. 11(a). The maximum macroscopic failure strength increases indicating a more brittle type of failure with increase in the interface strength. As shown in the inset of Fig. 11(a), for lower values of $\hat{\sigma}_c$, failure type is completely cohesive with parti-

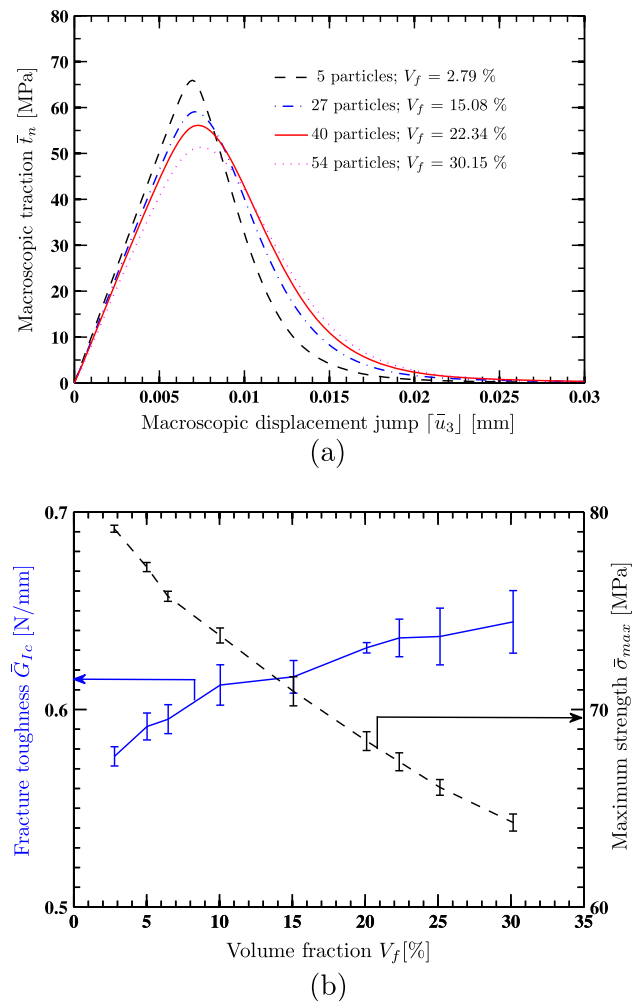


Fig. 10. Effect of volume fraction on the macroscopic traction-separation law (a) and macroscopic fracture toughness and failure strength (b).

cle debonding, while higher values of the interface strength preclude debonding and direct the microcracks

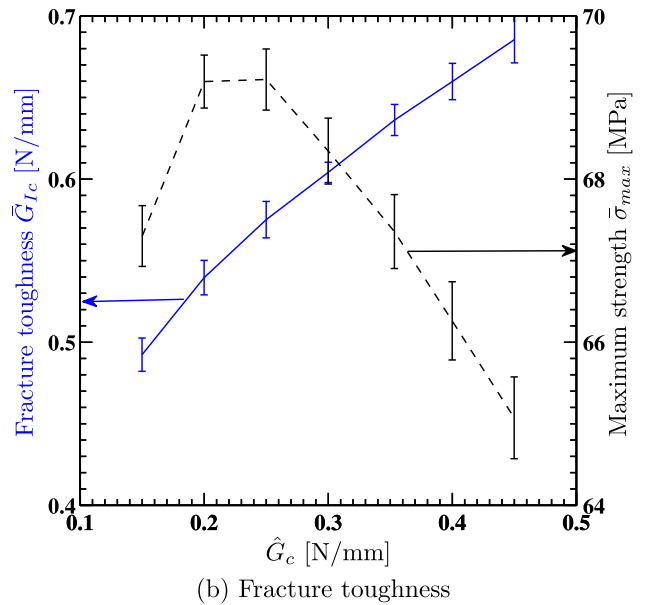
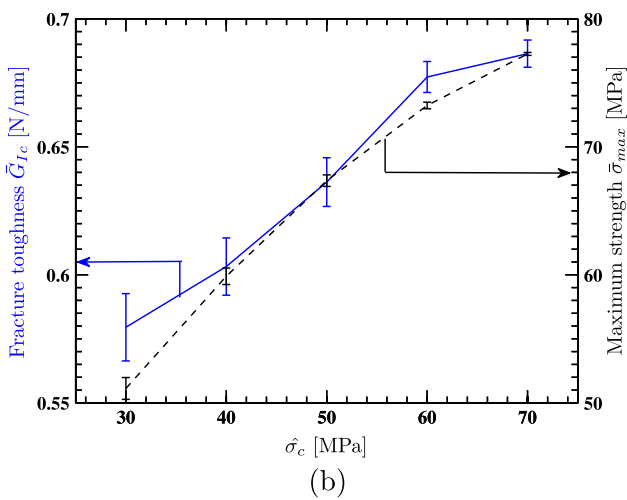
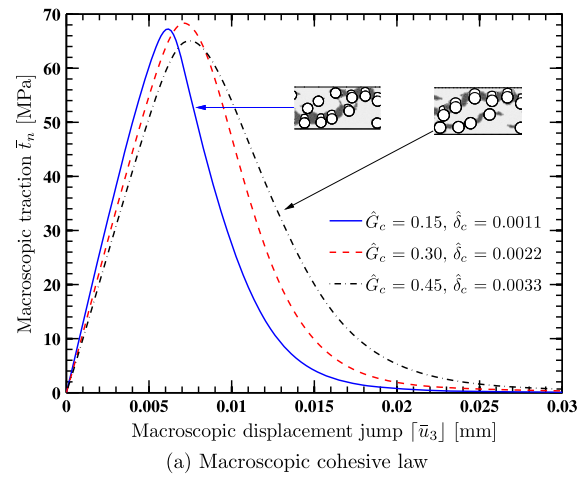
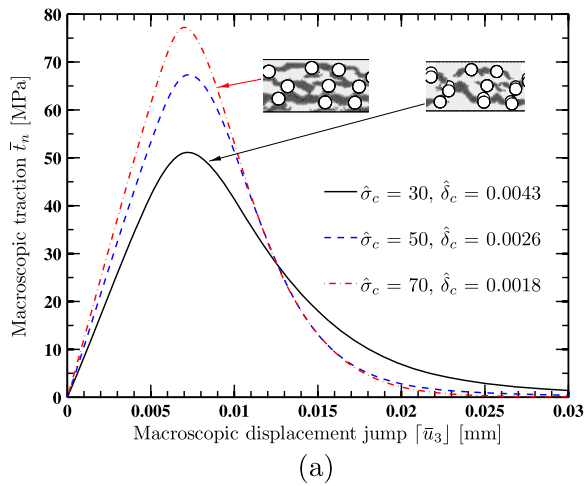


Fig. 11. Effect of microscopic interfacial failure strength $\hat{\sigma}_c$ (at constant fracture toughness \hat{G}_c) on macroscopic traction–separation law (a) and macroscopic fracture toughness and failure strength (b). The inset of (a) shows details of the failure processes at the micro-scale. Units for $\hat{\sigma}_c$ and $\hat{\delta}_c$ in (a) are MPa and mm, respectively.

Fig. 12. Effect of particle–matrix interfacial fracture toughness \hat{G}_c on the (a) macroscopic traction–separation law and (b) fracture toughness and failure strength. The inset of (a) shows details of the failure processes at the micro-scale. Units for \hat{G}_c and $\hat{\delta}_c$ in (a) are N/mm and mm, respectively.

away from the inclusions resulting in an adhesive–cohesive type of failure. The value of macroscopic displacement jump ($[\bar{u}_3]$) at which maximum macroscopic strength ($\bar{\sigma}_{max}$) occurs appears to be independent of the critical displacement jump $\hat{\delta}_c$. Lower values of interface strength result in a prolonged failure of the heterogeneous adhesive. The effect on the macroscopic fracture toughness and failure strength is further studied in Fig. 11(b). Both macroscopic fracture toughness and maximum strength increase by making the particle–matrix interface stronger resulting in increase in the amount of damage in the matrix. However, both would saturate as the perfect particle–matrix interface limit is approached, which is apparent from flattening of both the curves for $\hat{\sigma}_c > 60$.

The effect of variation of particle–matrix interface toughness, \hat{G}_c , is shown in Fig. 12(a), while keeping the critical interface strength constant ($\hat{\sigma}_c = 50$ MPa). A brittle interface is characterized by an overall brittle macroscopic failure in the heterogeneous adhesive. Increasing the microscopic interfacial fracture toughness improves the macroscopic fracture toughness by prolonging the failure

processes in the adhesive film. Unlike in the previous case, changing the microscopic interfacial fracture toughness \hat{G}_c affects not only the value of the peak cohesive traction but also the critical value of the displacement jump \bar{u}_3 at which that peak occurs. Increasing the energy needed to fail the particle–matrix interface leads to a corresponding increase in the macroscopic effective fracture toughness \bar{G}_{Lc} of the adhesive layer (Fig. 12(b)). This increase is associated not only with the additional energy dissipated along the inclusion–matrix interface but also in the amount of damage in the matrix, resulting in a non-linear relation between \bar{G}_{Lc} and \hat{G}_c .

The macroscopic failure strength $\bar{\sigma}_{max}$, on the other hand, has a non-monotonic dependence on \bar{G}_c , reaching a maximum of about 69.4 MPa for $\hat{G}_c \approx 0.25$ N/mm before decreasing with increasing \hat{G}_c . In all the cases, the damage in the heterogeneous adhesive layer starts in the matrix due to the particle–matrix or particle-to-particle interac-

tion. For more brittle particle–matrix interfaces (lower values of \widehat{G}_c), this initial matrix damage is augmented by the stress concentration present at the tips of particle–matrix interface cracks, which are active only for a short time after their critical opening is reached. These two effects lead to localization in the matrix, resulting at the macro-scale in a lower peak cohesive traction. For more ductile interfaces (higher values of \widehat{G}_c), the delayed failure of the interfaces reverses the synergy between particle–matrix interaction and interfacial cracks that can take larger opening before failure. In that case, the stress concentration due to the localized matrix failure promotes the interfacial failure, again leading to a lower value of $\bar{\sigma}_{max}$. For intermediate values of \widehat{G}_c , these two effects compete, resulting in an optimum value of the macroscopic failure strength $\bar{\sigma}_{max}$. In addition to the competition between particle–matrix interaction and interfacial cracks, the penalty type cohesive model might also attribute towards such behavior.

6. Conclusions

A multi-scale cohesive scheme has been used to study the failure processes occurring at the micro-scale in heterogeneous adhesives and their effect on the macroscopic cohesive response. A study of the RVE size has shown that the microscopic domain width has to be about 2 or 3 times the layer thickness for the macroscopic response to be representative for the loading histories considered. The effect of particle size, volume fraction and particle–matrix interfacial parameters on the failure response and effective macroscopic properties has been analyzed. In contrast to the perfect particle–matrix interface case, where the failure is of adhesive–cohesive nature, a weak interface between the constituents generally results in a cohesive type of failure. The presented response curves (Figs. 5(b), 10(b), 11(b), and 12(b)) could be used as design diagrams to yield a potentially new heterogeneous adhesive with desired macroscopic properties.

Acknowledgments

The authors gratefully acknowledge the support from the National Science Foundation for this work under Grant No. CMS 0527965. The authors also acknowledge the support from the Center for Simulation of Advanced Rockets (CSAR) at the University of Illinois, Urbana-Champaign. Research at CSAR is funded by the US Department of Energy as a part of its Advanced Simulation and Computing (ASC) program under Contract No. B523819.

References

Chen, X.-H., Mai, Y.-W., 1998. Micromechanics of rubber-toughened polymers. *Journal of Material Science* 32, 3529–3539.
Gent, A., 1980. Detachment of an elastic matrix from a rigid spherical inclusion. *Journal of Material Science* 15.

Geubelle, P.H., Baylor, J., 1998. Impact-induced delamination of composites: a 2D simulation. *Composites B* 29B, 589–602.
Gitman, I., Askes, H., Sluys, L., 2007. Representative volume: existence and size determination. *Engineering Fracture Mechanics* 74, 2518–2534.
Hill, R., 1972. On constitutive macro-variables for heterogeneous solids at finite strain. *Proceedings of the Royal Society London, Series A* 326, 131–147.
Hsiao, K.-T., Alms, J., Advani, S., 2003. Use of epoxy/multiwalled carbon nanotubes as adhesives to join graphite fibre reinforced polymer composites. *Nanotechnology* 14, 791–793.
Johnsen, B., Kinloch, A., Mohammed, R., Taylor, A., Sprenger, S., 2007. Toughening mechanisms of nanoparticle modified epoxy polymers. *Polymer* 48, 530–541.
Kawaguchi, T., Pearson, R., 2003a. The effect of particle–matrix adhesion on the mechanical behavior of glass-filled epoxies. Part 1. Study on yield behavior and cohesive strength. *Polymer* 44, 4229–4238.
Kawaguchi, T., Pearson, R., 2003b. The effect of particle–matrix adhesion on the mechanical behavior of glass-filled epoxies. Part 2. A study on fracture toughness. *Polymer* 44, 4239–4247.
Kinloch, A., 2003. Toughening epoxy adhesives to meet today's challenges. *MRS Bulletin* 28 (6), 445–448.
Kitey, R., Tippur, H., 2005a. Role of particle size and filler–matrix adhesion on dynamic fracture of glass filled epoxy I macromechanisms. *Acta Materialia* 53, 1153–1165.
Kitey, R., Tippur, H., 2005b. Role of particle size and filler–matrix adhesion on dynamic fracture of glass filled epoxy II linkage between macro- and micro-measurements. *Acta Materialia* 53, 1167–1178.
Lange, F., 1970. The interaction of a crack front with a second-phase dispersion. *Philosophical Magazine* 22, 938–992.
Lubliner, J., 1972. On thermodynamic foundations of non-linear solid mechanics. *International Journal of Non-Linear Mechanics* 7, 237–254.
Lubliner, J., 1973. On the structure of the rate equations of materials with internal variables. *Acta Mechanica* 17, 109–119.
Matouš, K., Kulkarni, M., Geubelle, P., 2008. Multiscale cohesive failure modeling of heterogeneous adhesives. *Journal of the Mechanics and Physics of Solids* 56, 1511–1533.
Miehe, C., 2002. Strain-driven homogenization of inelastic microstructures and composites based on an incremental variational formulation. *International Journal For Numerical Methods in Engineering* 55, 1285–1322.
Nakamura, Y., Okabe, S., Iida, T., 1999. Effects of particle shape, size and interfacial adhesion on the fracture strength of silica-filled epoxy resin. *Polymers and Polymer Composites* 7, 177–186.
Needleman, A., 1990b. An analysis of decohesion along an imperfect interface. *International Journal of Fracture* 42, 21–40.
Nicholson, D., 1979. On the detachment of a rigid inclusion from an elastic matrix. *Journal of Adhesion* 10, 255–260.
Ortiz, M., Pandolfi, A., 1999. Finite-deformation irreversible cohesive elements for three-dimensional crack-propagation analysis. *International Journal for Numerical Methods in Engineering* 44, 1267–1282.
Pearson, R., Yee, A., 1991. Influence of particle size and particle size distribution on toughening mechanisms in rubber-modified epoxies. *Journal of Material Science* 26, 3828–3844.
Pucciariello, R., Bianchi, N., Braglia, R., Garbassi, F., 1989. The morphology of rubber toughened epoxy adhesives. *International Journal of Adhesion and Adhesives* 9 (2), 77–82.
Simo, J., Ju, J., 1987a. Strain- and stress-based continuum damage models. I. Formulation. *International Journal of Solids and Structures* 23 (7), 821–840.
Simo, J., Ju, J., 1987b. Strain- and stress-based continuum damage models. II. Computational aspects. *International Journal of Solids and Structures* 23 (7), 841–869.
Spanoudakis, J., Young, R., 1984a. Crack propagation in a glass particle-filled epoxy resin. Part 1. Effect of particle volume fraction and size. *Journal of Materials Science* 19, 473–486.
Spanoudakis, J., Young, R., 1984b. Crack propagation in a glass particle-filled epoxy resin. Part 2. Effect of particle–matrix adhesion strength. *Journal of Materials Science* 19, 487–496.